The Coupled GCM ECHO-2. Part II: Indian Ocean Response to ENSO

STEPHAN VENZKE, MOJIB LATIF, AND ANDREAS VILLWOCK

Max-Planck-Institut für Meteorologie, Hamburg, Germany

(Manuscript received 29 October 1997, in final form 17 June 1999)

ABSTRACT

The interannual variability of the Indian Ocean SST is investigated by analyzing data from observations and an integration of a global coupled GCM (CGCM) ECHO-2. First, it is demonstrated that the CGCM is capable of producing realistic tropical climate variability. Second, it is shown that a considerable part of the interannual variability in Indian Ocean SST can be described as the response to interannual fluctuations over the Pacific related to ENSO. Although the Indian Ocean region also exhibits ENSO-independent interannual variability, this paper focuses on the ENSO-induced component only. Large-scale SST anomalies of the same sign as those observed in the eastern equatorial Pacific Ocean during ENSO extremes develop in the entire tropical and subtropical Indian Ocean with a time lag of about 4 months. This lead–lag relationship is found in both the observations and the CGCM. Using the CGCM output, it is shown that the ENSO signal is carried into the Indian Ocean mainly through anomalous surface heat fluxes.

1. Introduction

In the first part of this series, Frey et al. (1997) described the mean state, annual cycle, and interannual variability over the tropical Pacific as simulated by the second cycle of our coupled ocean–atmosphere general circulation model (CGCM), hereinafter referred to as ECHO-2. Several aspects of the improved model's performance over the Pacific Ocean with respect to the first version of the model, hereinafter referred to as ECHO-1, were discussed in Frey et al. (1997). The mean state, the annual cycle, and the interannual and decadal variability as simulated by ECHO-1 were investigated in several studies (Latif et al. 1994; Schneider et al. 1996; Latif and Barnett 1994, 1996; Grötzner et al. 1998). Modifications in the atmospheric convection scheme, a better representation of the low-level stratus clouds, and a new numerical scheme for active tracer advection in the ocean model improved the coupled model behavior. The latter results in a better simulation of the thermocline, causing the sea surface temperature (SST) to be more sensitive to thermocline perturbations and therefore leading to enhanced interannual variability in the coupled integration with ECHO-2.

Large-scale air–sea interactions play a crucial role in generating interannual variability in the Tropics. The classical example for such air–sea interactions is the El Niño–Southern Oscillation (ENSO) phenomenon, which is the strongest climate fluctuation on the short-range climatic timescale from a few months to several years [see the textbook of Philander (1990) for a good overview]. Because the ENSO signal is strongest in the tropical Pacific, much less attention has been paid so far to the interannual variabilities of the tropical Indian and Atlantic Ocean and only a few papers exist that address these issues. Several studies have addressed the interaction of interannual variability over the tropical Indian Ocean with the Asian monsoon. Shukla (1987) as well as Ju and Slingo (1995) found that stronger westerly winds associated with strong monsoon years tend to cool down the ocean surface in the northwest Indian Ocean and the Arabian Sea in the postmonsoon months. On the other hand, several studies (e.g., Webster and Yang 1992; Ju and Slingo 1995; Soman and Slingo 1997) suggest a clear relationship between the strength of the large-scale monsoon circulation and the phase of ENSO: years with warm SST anomalies in the central and east Pacific have a weaker monsoon circulation and a delayed onset. Opposite behavior is noted for those years with cold SST anomalies in the eastern equatorial Pacific Ocean. Latif and Barnett (1995) conclude from an investigation of several model integrations and observations that air–sea interactions in the Indian and Atlantic Ocean are much weaker than those in the Pacific Ocean but that they, nevertheless, contribute to the interannual variability in these regions, because they amplify the ENSO-induced signal. In particular, the SST anomalies in the tropical Pacific Ocean were found to force SST anomalies of the same sign in the Indian Ocean. In turn, there was no evidence that the Indian

Corresponding author address: Dr. Mojib Latif, Max-Planck-Institut für Meteorologie, Bundesstr. 55, 20146 Hamburg, Germany.
E-mail: latif@dkrz.de

Ocean can significantly affect the ENSO cycle. In line with these results are the findings of Kiladis and Diaz (1989), who describe an in-phase response of the tropical Indian Ocean SST to ENSO and suggest radiational forcing and local wind stress changes as possible causes.

In this study, we examine the ENSO response of the Indian Ocean by analyzing observations and the output of a 20-yr integration with our ECHO-2 CGCM. The paper is organized as follows: In section 2 a brief description of the coupled model and the simulated tropical mean state and the seasonality are given. The ENSO-related tropical variability is examined in section 3. In section 4, we derive the physical processes causing the Indian Ocean response to ENSO. The paper is concluded with a summary of our major findings in section 5.

2. Model description and tropical mean state

A detailed description of the CGCM ECHO-2 and especially the changes made in respect to the earlier version ECHO-1 was given in Part I of this series (Frey et al. 1997). Therefore, we restrict ourselves to a rather brief model description.

The coupled atmosphere–ocean model ECHO-2 is set up from cycle 4 of the Hamburg atmosphere GCM, (ECHAM; Roeckner et al. 1996) and the Hamburg Ocean Primitive Equation GCM, (HOPE; Wolff et al. 1997).

ECHAM-4 is a global low-order spectral model with a triangular truncation at wavenumber 42 (T42). The nonlinear terms and the parameterized physical processes are calculated on a 128 $\times$ 64 Gaussian grid, which yields a horizontal resolution of about 2.8° $\times$ 2.8°. There are 19 levels in the vertical that are defined on sigma surfaces in the lower troposphere and on p surfaces in the upper troposphere and the stratosphere.

ECHAM-4 is coupled to the HOPE model without applying flux correction. They interact over all three oceans in the region 60°N–60°S. Since we have not yet included a sea-ice model, the SSTs are relaxed to Levitus (1982) climatology poleward of 60°.

The ocean model is forced by the surface wind stress, the surface heat flux, and the freshwater flux simulated by the atmospheric model. It uses a realistic bottom topography. The model has a 2.8° resolution, with the meridional resolution gradually increased to 0.5° within the region 10°N–10°S. Vertically, there are 20 irregularly spaced levels, with 10 levels within the upper 300 m. As described in Latif et al. (1994), solar radiation is allowed to penetrate beneath the first ocean layer. The numerical scheme of the ocean model uses the Arakawa E-grid (Arakawa and Lamb 1977) with a 2-h time step.

The simulated SST is used to force the ECHAM model. The coupling is synchronous, with exchange of information every 2 h. A 360-day year subdivided in 12 equal-length months of 30 days is used. The coupled GCM is forced by seasonally varying insolation. The oceanic initial conditions are taken from Levitus (1982) climatology and those for the atmospheric model from a control run with climatological SSTs. The coupled integration is started on 1 January and continued for 20 yr. Pierce et al. (2000) carried the integration on for another 120 yr. Their results confirm that the decades analyzed in this paper are representative of the model's interannual variability. To avoid effects of the initialization we omit the first 2 yr of the integration in our analysis.

The SST is a key quantity by which the performance of coupled models can be evaluated. In Fig. 1 we display the tropical annual-mean SSTs as simulated in our coupled model integration and the mean observed tropical SSTs as derived from the SST dataset of the U.K. Meteorological Office (UKMO), which is referred to as the Global Sea-Ice and Sea Surface Temperature (GISST) dataset, for the period 1949–91. At this point it shall be mentioned that the simulated SST represents the temperature of the top model layer (i.e., upper 20 m). The simulation with ECHO-2 shows a cold bias in the equatorial Pacific. However, the warm pool/cold tongue structure is simulated with more success by the new version of the model, since the numerical effective diffusion in the ocean model is reduced. In the Indian Ocean the observed mean state of the SSTs is fairly well reproduced by our coupled GCM.

As shown in Fig. 2, the annual-mean wind stress is also realistically simulated in ECHO-2. Over the southern tropical Indian Ocean we find southeasterly trade winds of equal strength and orientation as those derived for 1949–91 from the Comprehensive Ocean–Atmosphere Data Set (COADS; da Silva et al. 1994). Westerly winds with similar strength are found north of the equator in both the observations and our CGCM integration. Only the wind stresses over the Arabian Sea are not properly simulated by ECHO-2. As can be seen in Fig. 3, this deficiency has to be attributed to an overestimation of the northeasterly winds in winter, which seems to be due to the simulation of too cold air temperatures over Siberia by the ECHAM-4 model. Otherwise, the monsoon circulation over the Arabian Sea is simulated quite well by the coupled GCM, both in terms of phase and amplitude (Fig. 3c). As a result of too strong winds over the Arabian Sea in winter (December–February, hereafter DJF) the latent heat loss is enhanced in winter (DJF), which leads to colder than observed SSTs in this area during late winter and spring (Fig. 3d). Apart from a slightly delayed onset of the summer monsoon, however, these SST errors appear not to affect the quality of the simulated monsoon circulation. Furthermore, the associated seasonal variations of the surface currents are well simulated (Fig. 4). As in Murtugudde et al. (1996), the reversal of the Somali Current from February to August is clearly seen in the model results. Due to the coarser zonal resultion, the speed of the Somali Current is significantly lower than in Murtugudde et al. (1996). The seasonality of the South Equatorial Counter Current, which is fed by the southward Somali Current in

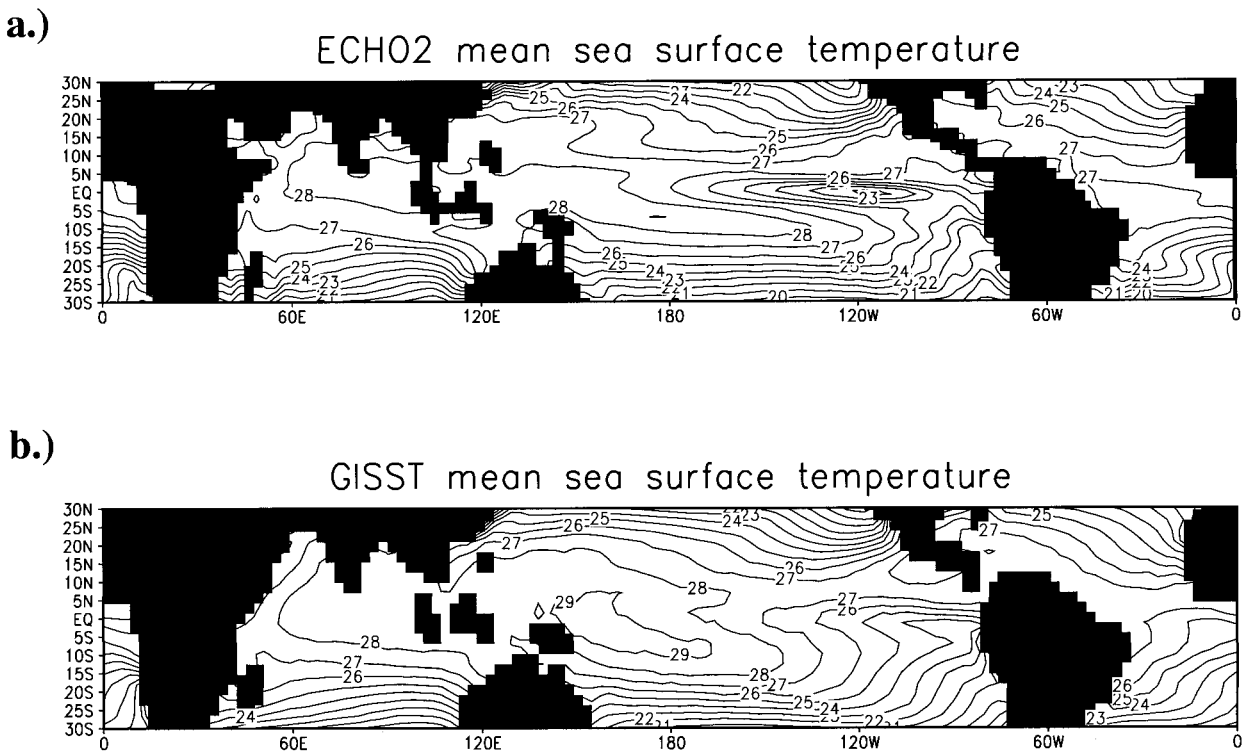

FIG. 1. Tropical annual-mean SSTs (°C) (a) as simulated by the CGCM ECHO-2 and (b) as observed.

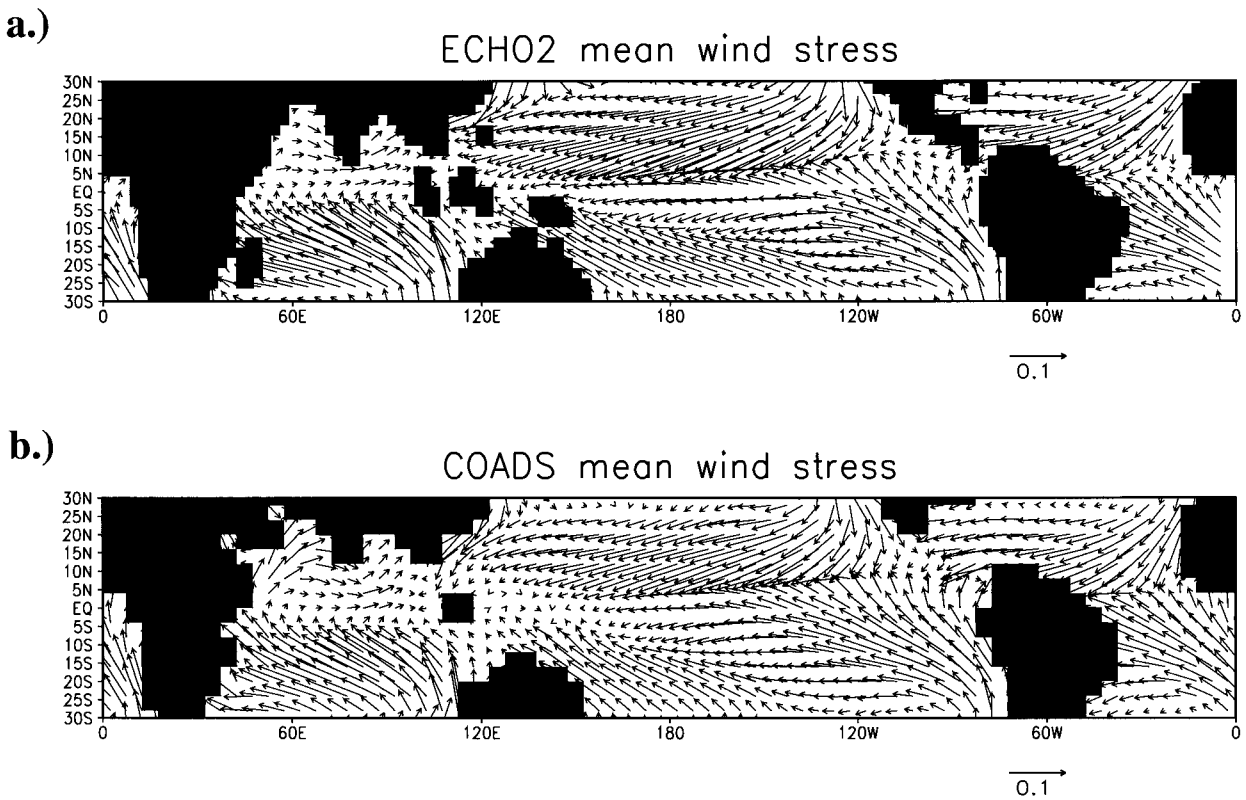

FIG. 2. Tropical annual-mean wind stress (Pa) (a) as simulated by the CGCM ECHO-2 and (b) as observed.

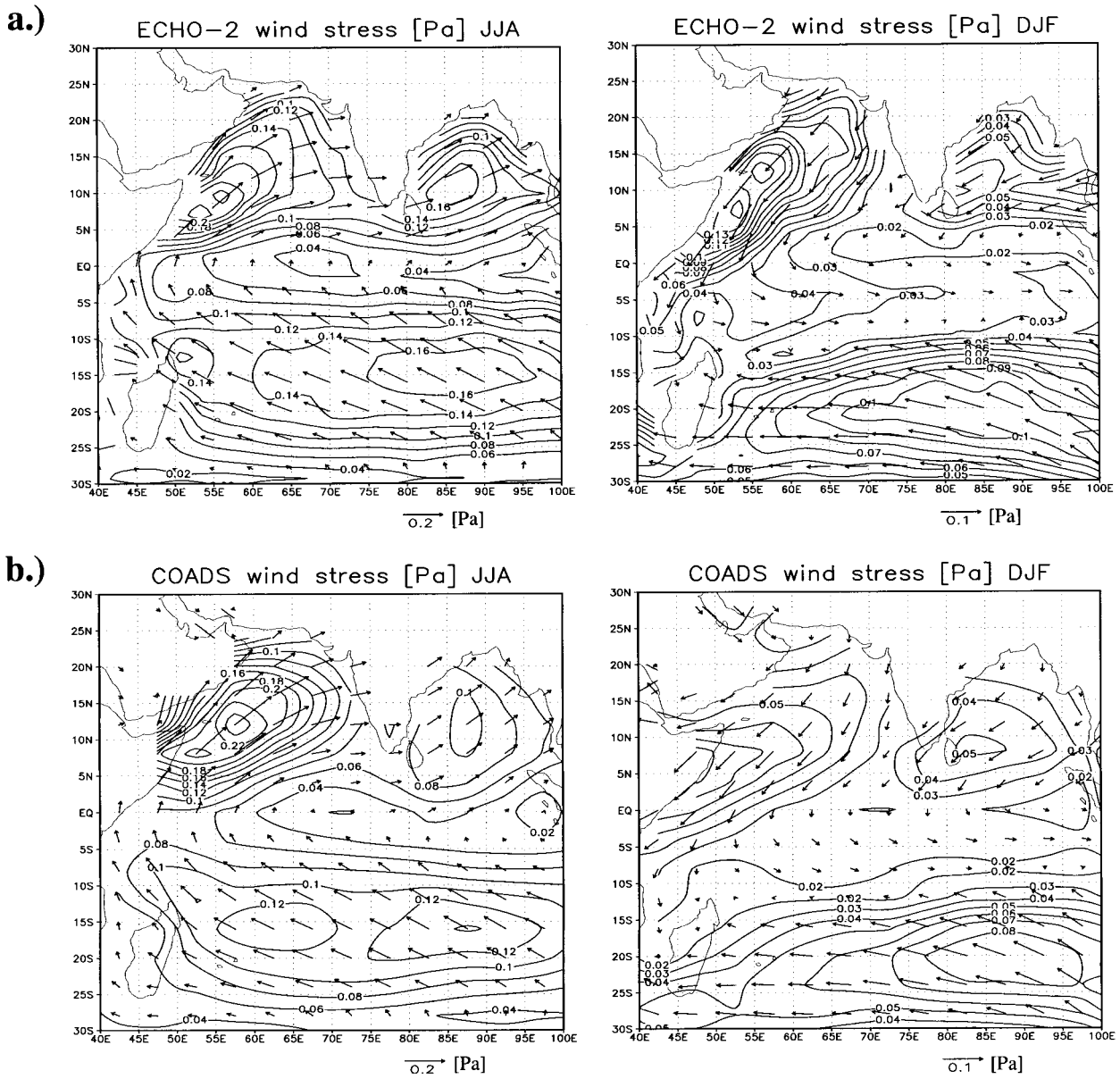

FIG. 3. Climatological seasonal-mean surface wind stress (Pa) for boreal summer (Jun–Aug) and winter (Dec–Feb) (a) as simulated by the CGCM ECHO-2 and (b) as observed.

February, and of the South Equatorial Current are also in agreement with the results of Murtugudde et al. (1996). During the transition periods of the monsoon, the model produces a wind-driven eastward equatorial jet (Wyrtki 1973) that peaks around May and appears again in December. The latter maximum is late by more than a month compared to the observations of Reverdin (1987), which is due to a phase error of the zonal winds on the equator as discussed below. Furthermore, the seasonal reversal of the flow direction in the Bay of Bengal and south of Sri Lanka is well captured by the ECHO-2 model.

Details about the annual-mean state and the annual cycle in the tropical Pacific as well as a comparison of the integration of ECHO-2 with earlier integrations of ECHO-1 are given in Part I of this series (Frey et al. 1997). In this part, we shall investigate the interannual variablity in the ECHO-2 integration and focus on the Indian Ocean response to ENSO.

3. ENSO-related tropical variability

The most apparent improvement relative to the simulation with the previous model version ECHO-1 is the enhanced level of interannual variability in ECHO-2. To emphasize the interannual fluctuations, the anomalies

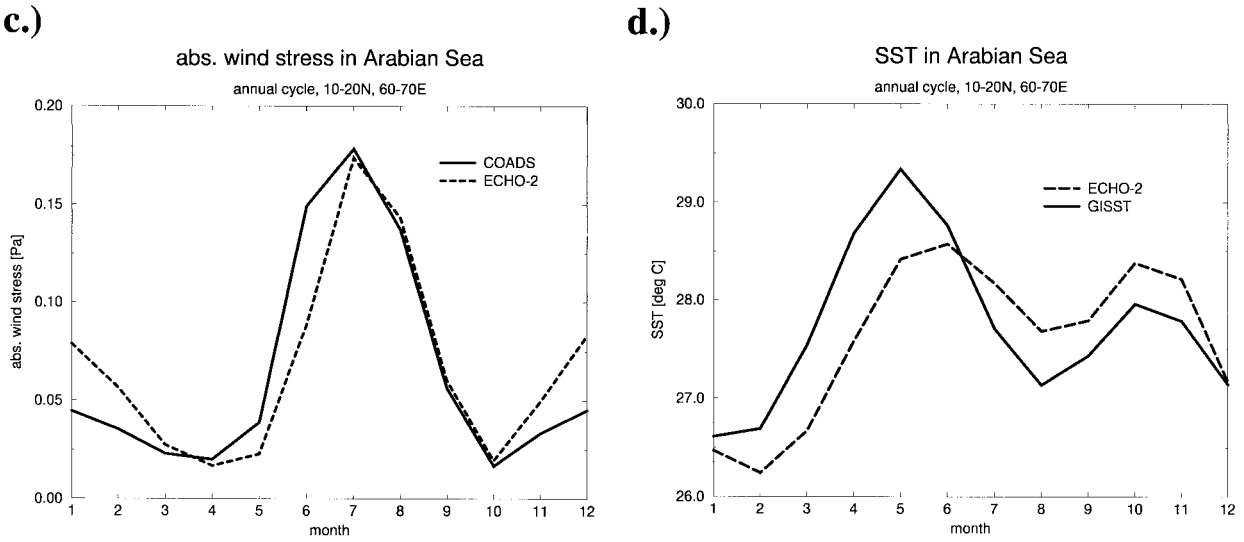

FIG. 3. (*Continued*) (c) Seasonality of the simulated and observed wind stress over the Arabian Sea (Pa) averaged over 10°–20°N and 60°–70°E. (d) Same as (c) but for SST (°C).

have been slightly smoothed using a 13-month running mean filter. This, however, does not effect any of the qualitative results of this paper. The model simulates, for instance, interannual SST anomalies in the equatorial Pacific (Figs. 5 and 6). In comparison with observations, the amplitude of these anomalies is roughly a factor of two too small (note the scale in Fig. 5) and the period is slightly too short. However, the interannual variability is simulated more realistically than in the ECHO-1 model. This is due to a better simulation of the thermocline, which has been achieved by changing the numerical treatment of tracer advection. Considerably less effective mixing inhibits an erosion of the thermocline making the SST more sensitive to thermocline perturbations in the eastern equatorial Pacific and therefore enhancing the interannual variability in this region in the coupled run with ECHO-2.

The spatial structures of the interannual SST anomalies and the associated wind stress anomalies are shown in Figs. 6 and 7, respectively. Overall, the anomaly structures are simulated reasonably well, with SST anomalies centered in the eastern equatorial Pacific, accompanied by westerly wind stress anomalies in the western equatorial Pacific. In agreement with the ob-

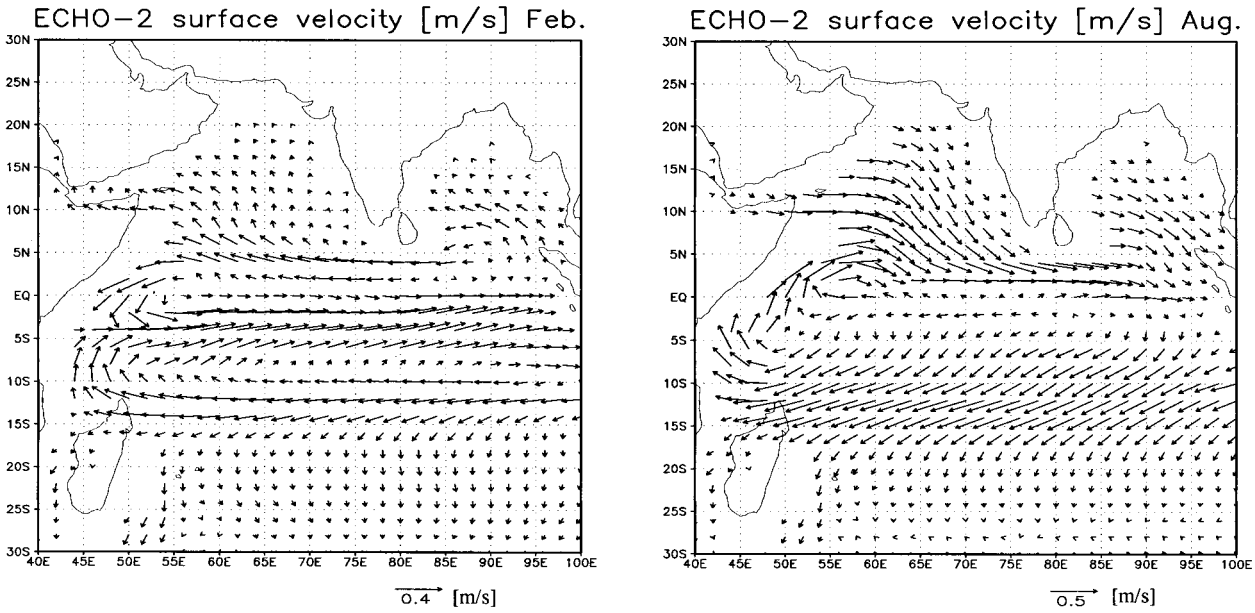

FIG. 4. Simulated climatological mean surface currents (m s^{-1}) for Feb and Aug.

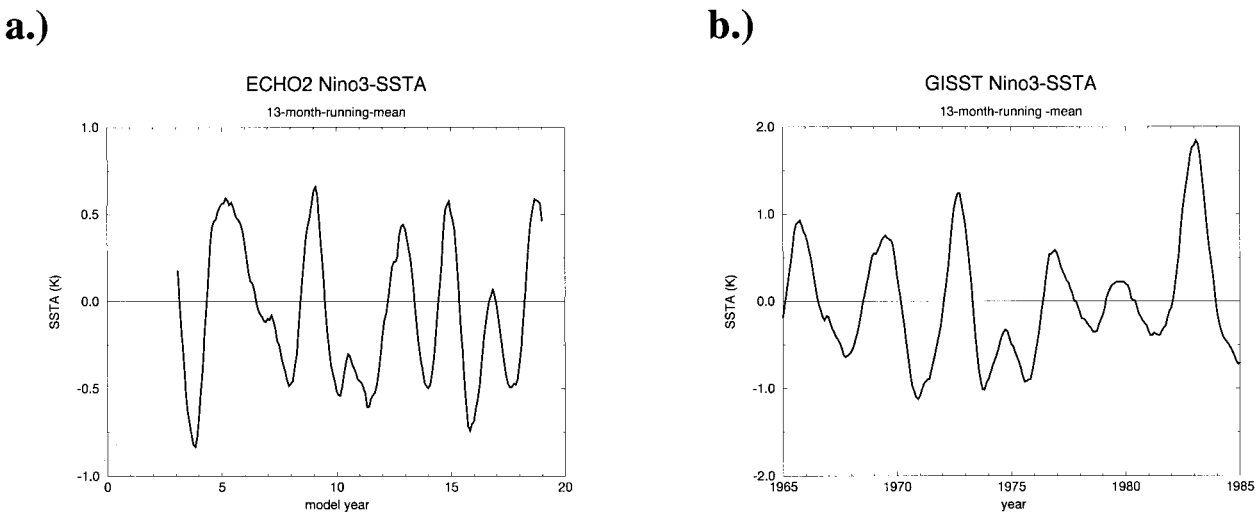

FIG. 5. Time series of (a) model-simulated and (b) observed SST anomalies averaged over the Niño-3 index region (5°S–5°N, 150°–90°W). The data were smoothed using a 13-month running mean filter.

servations, large-scale SST anomalies of the same sign as those in the eastern equatorial Pacific and associated westward wind stress anomalies in the equatorial Indian Ocean are simulated by ECHO-2. There are, however, some differences between the simulation and observations. The simulated SST anomalies are too much equatorially confined, and they extend too far into the western Pacific. The latter deficiency is related to the cold tongue, which is too strong and extends too far into the western Pacific. Furthermore, the coupled model underestimates the strength of the off-equatorial SST anomalies of opposite sign in the Pacific. The reason for these errors seems to be inherent to the ocean model, since the problems in simulating the ENSO related SST

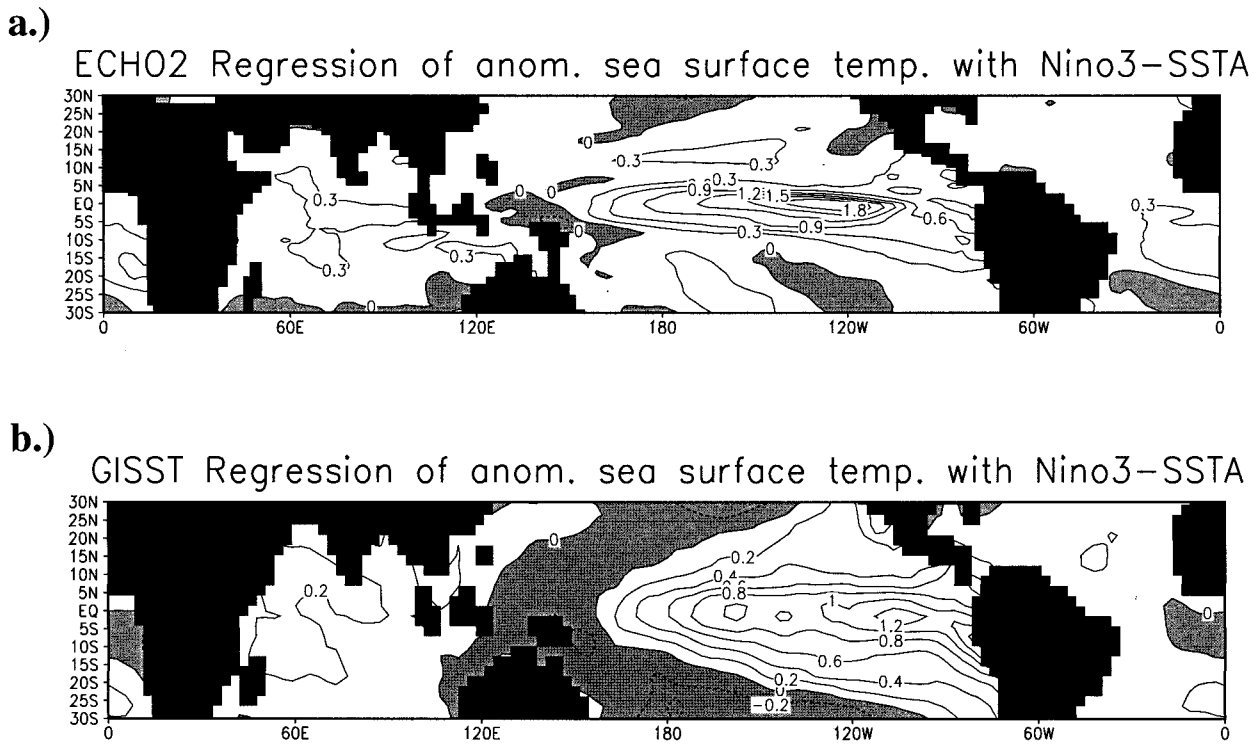

FIG. 6. Spatial distribution of SSTA regression coefficients relative to the Niño-3 index time series as derived from (a) the integration of the CGCM ECHO-2 and (b) observations (1949–91). The data were smoothed using a 13-month running mean filter prior to the analysis.

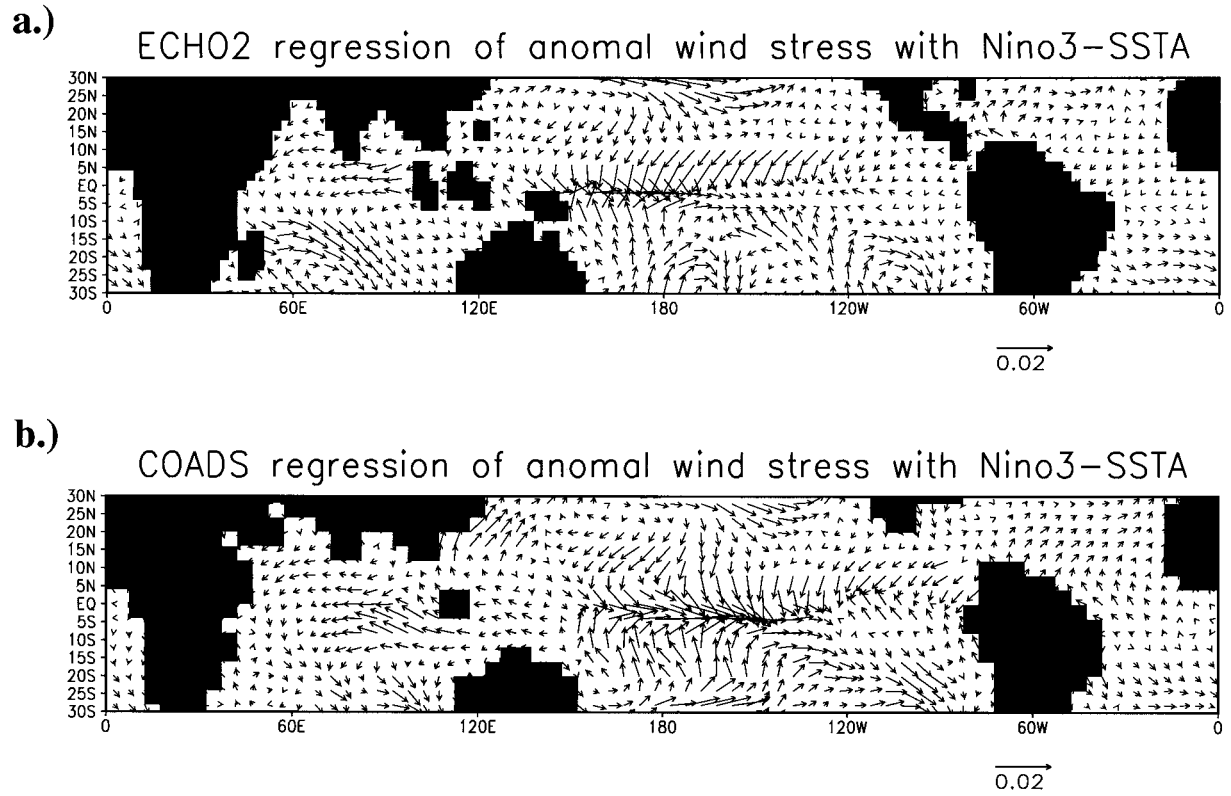

FIG. 7. Same as Fig. 6 but for the regression of anomalous wind stress relative to the Niño-3 index time series of SSTA (Pa K^{-1}).

anomalies also occur in uncoupled runs with our ocean model forced by observed wind stresses and heat fluxes.

In summary, our coupled GCM ECHO-2 simulates the ENSO phenomenon in the tropical Pacific reasonably well and furthermore exhibits in the Indian Ocean region similar ENSO-related SST and wind stress anomalies as those found in observations.

4. Causes of the Indian Ocean SST response to ENSO

The only oceanic parameter with sufficient data coverage in space and time that can be used to study the interannual variability in the Indian Ocean is the SST. Before we investigate the causes of the Indian Ocean SST response to ENSO in our integration with ECHO-2, we need to prove that it really is a response and therefore have to identify a temporal relationship between the equatorial eastern Pacific and Indian Ocean SSTs in our CGCM integration as well as in observations. In Fig. 8, time series of tropical Indian Ocean (20°N–20°S, 50°–100°E) and equatorial eastern Pacific Ocean (Niño-3: 5°S–5°N, 150°–90°W) SST anomalies as inferred from observations and the CGCM integration are shown together with their corresponding cross-correlation functions. Note that the amplitude of the simulated signal is smaller than that observed by a factor of 2. The Niño-3 time series will be used as an ENSO index throughout the text. Consistently, we find in the observations and in the integraton with ECHO-2 maximum cross correlation ($\tau_{obs} = 0.85$, $\tau_{echo\text{-}2} = 0.60$) when the Indian Ocean SST variations lag those of the eastern Pacific SST by about 4 months. The spatial structure of the Indian Ocean SST anomaly field at this lag can be inferred from Fig. 9. Overall, the interannual Indian Ocean SST variations are positively correlated with the eastern equatorial Pacific Ocean SST anomalies. The correlations are strongest in the tropical region, and similar correlation patterns are found in both the model integration and in observations. Furthermore, these findings about the spatial structure and temporal evolution of the ENSO-related interannual variability in the Indian Ocean are in agreement with earlier studies. Villwock (1994) obtained similar results by applying the empirical orthogonal function (EOF) technique to the Indian Ocean SST dataset of Reynolds (1988). The associated time series of the dominant EOF (explaining locally up to 60% of the total variance) was found to be strongly anticorrelated with the Southern oscillation index (SOI) at a lag of 3 months, with the SOI leading. The study of Nicholls (1989) also confirms our findings. Thus, the ENSO signal is a significant part of the interannual variability in the Indian Ocean. Variations in the SST in the eastern tropical Pacific Ocean are followed by large-scale SST anomalies of the same sign in the Indian Ocean with a time lag of about 4 months. These features

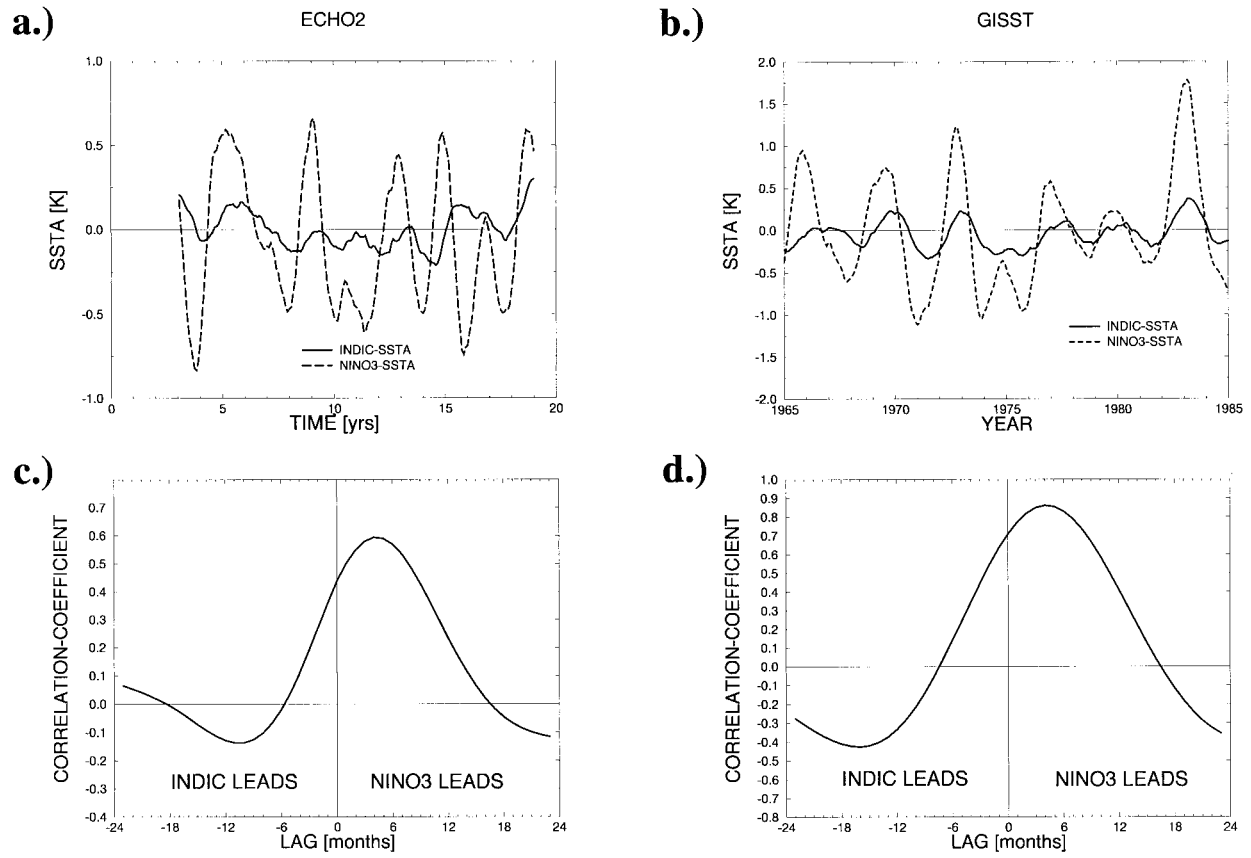

FIG. 8. Time series of Indian Ocean (averaged over 20°N–20°S, 50°–100°E) and Niño-3 SST anomalies (°C) as (a) simulated with ECHO-2 and (b) observed. The corresponding cross-correlation functions for the simulation (c) and observations (d) are shown below. The data were smoothed using a 13-month running mean filter.

are simulated realistically by our CGCM ECHO-2, and we shall use it to explore the physics of the Indian Ocean response to ENSO.

Villwock (1994) investigated different atmospheric variables such as upper- and low-level winds, outgoing longwave radiation (OLR), and cloud cover in a combined EOF analysis of these quantities, taken from National Meteorological Center (NMC) analysis for the period 1975–85. The ENSO-related wind patterns were found to be dominated by upper-level westerlies and

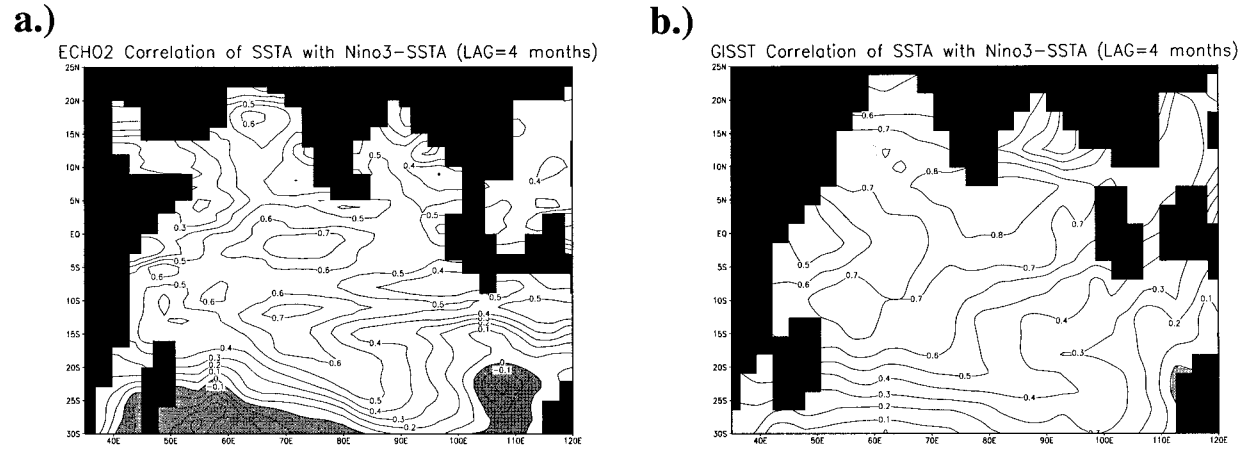

FIG. 9. Spatial distribution of correlation coefficients of Indian Ocean SSTA with Niño-3 SSTA at a lag of 4 months, with Niño-3 leading, as (a) simulated with ECHO-2 and (b) observed. The data were smoothed using a 13-month running mean filter prior to the analysis.

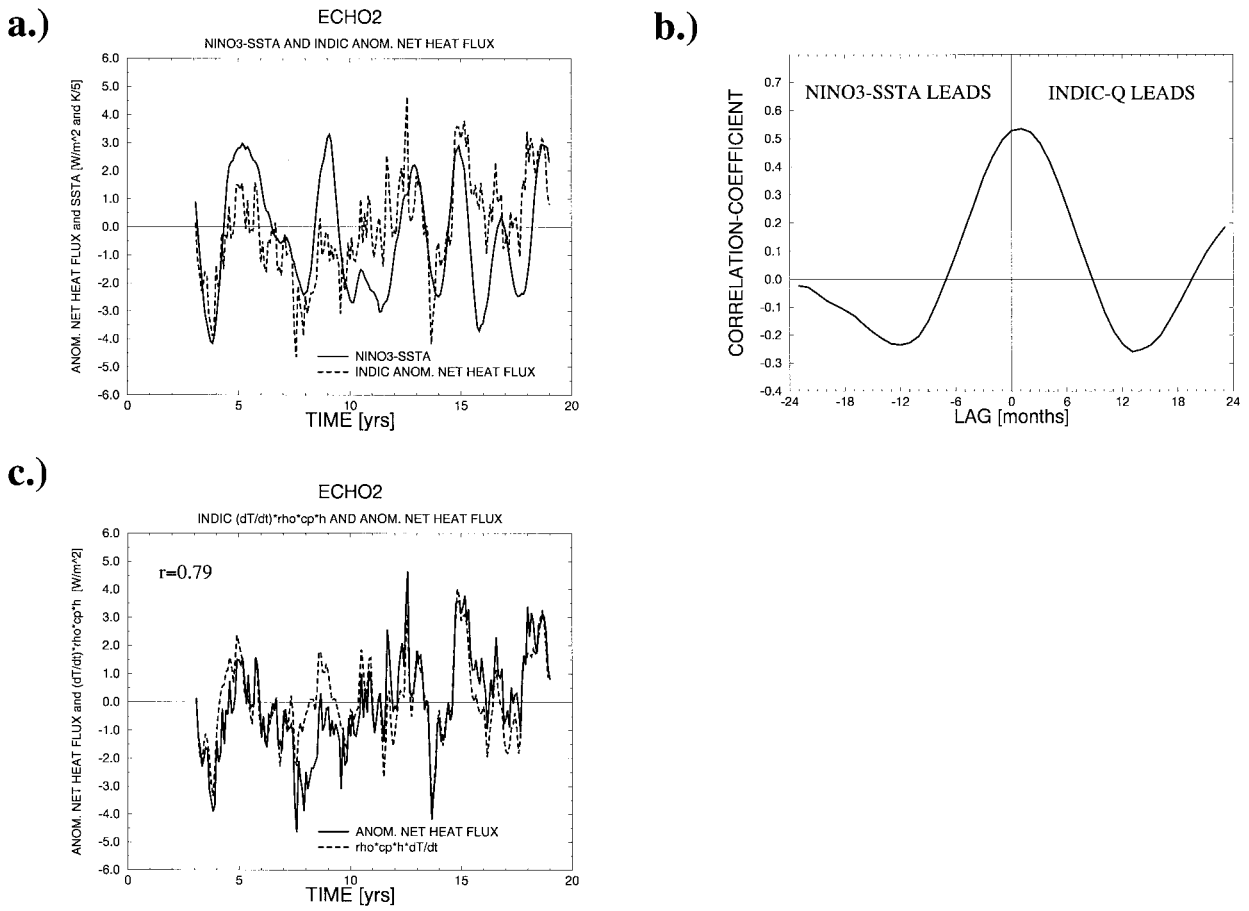

FIG. 10. (a) Time series of model-simulated Niño-3 SSTA (°C) and Indian Ocean (averaged over 20°N–20°S, 50°–100°E) anomalous net surface heat flux (W m^{-2}). (b) The corresponding cross-correlation function. (c) Indian Ocean (averaged over 20°N–20°S, 50°–100°E) time derivative of SSTA multiplied by $\rho = 1023$ kg m^{-3}, $c_p = 3980$ J (kg K)$^{-1}$, and $h = 50$ m together with anomalous net surface heat flux (W m^{-2}). The data were smoothed using a 13-month running mean filter prior to the analysis.

low-level easterlies in the central to eastern equatorial Indian Ocean region (see Fig. 7). Furthermore, the ENSO response patterns of the OLR and the cloud cover were found to be characterized by a dipole structure, corresponding to reduced convection in the eastern Indian Ocean and enhanced convection west of 80°E. However, due to the lack of accurate observational data, the exact relative importance of the different components that may induce the ENSO signal in the Indian Ocean SST could not be determined.

The results from the integration of the ECHO-2 model now provide a comprehensive dataset with which we can carry out this investigation. As the response time of the large-scale Indian Ocean SST to the eastern Pacific SST variations is only about 4 months, changes in the atmospheric circulation are most likely to be responsible for the transmission of the ENSO signal. Changes of the SST may occur as a consequence of changed surface heat flux, changed mixing in the upper ocean, or changed vertical advection. Changes in horizontal advection are only likely to be of importance where horizontal temperature gradients exist. As those are not very strong in the area where the main ENSO-induced signal is found (Figs. 1 and 9), we study the contribution of surface heat flux changes first. Figure 10a shows the temporal evolution of the anomalous net surface heat flux averaged over the Indian Ocean index region. It exhibits nearly in-phase variations with the corresponding Niño-3–SST anomalies (SSTAs) time series, indicating that the ENSO-induced part of the interannual variability of the Indian Ocean SST may be due to anomalous surface heat flux forcing. This becomes even more evident from Fig. 10c. It shows that the changes of large-scale SST anomalies in the tropical and subtropical Indian Ocean can almost completely be attributed to anomalous surface heat flux forcing. The cross-correlation function (Fig. 10b) reveals that the Indian Ocean surface heat flux anomalies are related to equatorial Pacific SST anomalies. The in-phase correlation between the Indian Ocean surface heat flux anomalies and the Niño-3 SSTAs is significant at the 95% confidence level. Overall, these results show that the large-scale ENSO-related SST variability in the Indian

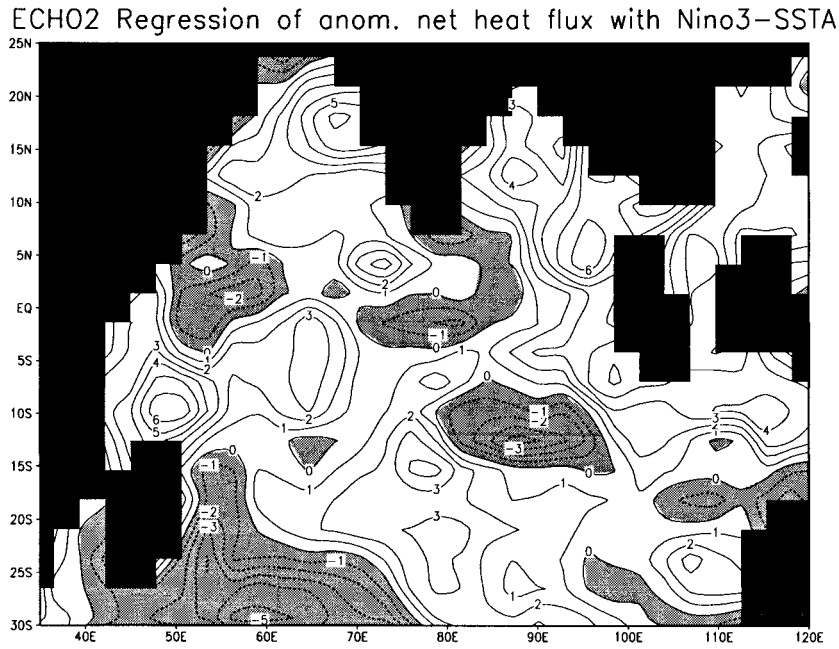

FIG. 11. Spatial distribution of regression coefficients [W $(m^2 K)^{-1}$] of anomalous net surface heat flux over the Indian Ocean relative to Niño-3 SSTA. The data were smoothed using a 13-month running mean filter prior to the analysis.

Ocean arises in response to ENSO-induced net surface heat flux anomalies.

In Fig. 11, the spatial structure of the ENSO-induced anomalous net surface heat flux can be seen. The pattern is characterized by large-scale anomalous heat fluxes going into the ocean. In the central equatorial region, however, the ENSO-induced changes in the surface heat flux seem not to force the SST changes. This is somewhat surprising as the SST response to ENSO appeared to be rather strong in this region. We shall address this point later. Now, we shall have a more detailed look at the various components of the net surface heat flux. Patterns of the anomalous solar, thermal, latent, and sensible surface heat fluxes regressed upon the Niño-3-SSTA are shown in Fig. 12. Most striking in all components is the northeast–southwest dipole structure similar to the one found by Villwock (1994) in observed OLR and cloud cover.

As the area of strong convection over Indonesia moves eastward during the warm phase of the ENSO cycle, the solar heat flux (Fig. 12a) into the eastern Indian Ocean increases and warms the ocean. In contrast to the solar radiation, the longwave radiation is only marginally affected by changes in the convection because of the high moisture content of the atmospheric boundary layer in the Tropics (Webster 1990). The thermal heat loss of the eastern Indian Ocean therefore increases only slightly during a warm ENSO phase (Fig. 12b). Thus, the net effect of the reduced convection during the ENSO warm phase will be a heating of the eastern Indian Ocean. Our result is consistent with satellite data analysis by Chertock et al. (1991), who estimated a net surface radiation anomaly of about 5–10 W m^{-2} in the eastern Indian Ocean during warm ENSO phases.

Changes in the wind speed over the Indian Ocean, as those associated with ENSO extremes (Fig. 7), will also affect the surface heat flux. Especially, the latent heat flux critically depends on the surface wind speed. Comparing the patterns of ENSO-related anomalous wind stress (Fig. 7) and latent heat flux (Fig. 12c) indeed indicates that during warm ENSO extremes the latent heat loss is reduced in those regions where the wind stress magnitude (and by implication wind speed) is reduced. Those regions are in the central north-equatorial Indian Ocean and the area of the southeasterly trade winds. The anomalous sensible heat flux (Fig. 12d) is of minor importance.

In conclusion, the anomalous ENSO-related surface heat flux forcing may overall well explain the large-scale changes of the Indian Ocean SSTs that occur about 4 months after the Niño-3–SSTAs in our model. In the eastern part of the basin the solar component dominates, while in the central part the latent heat flux contributes most.

However, as noted above, in the central equatorial region the ENSO-related interannual SST signal is strong but cannot be fully explained by anomalous surface heat flux forcing (Fig. 11). We therefore investigate the anomalous wind stress forcing in that region in more detail. The meridional wind stress component at the equator is dominated by the annual monsoon cycle. The

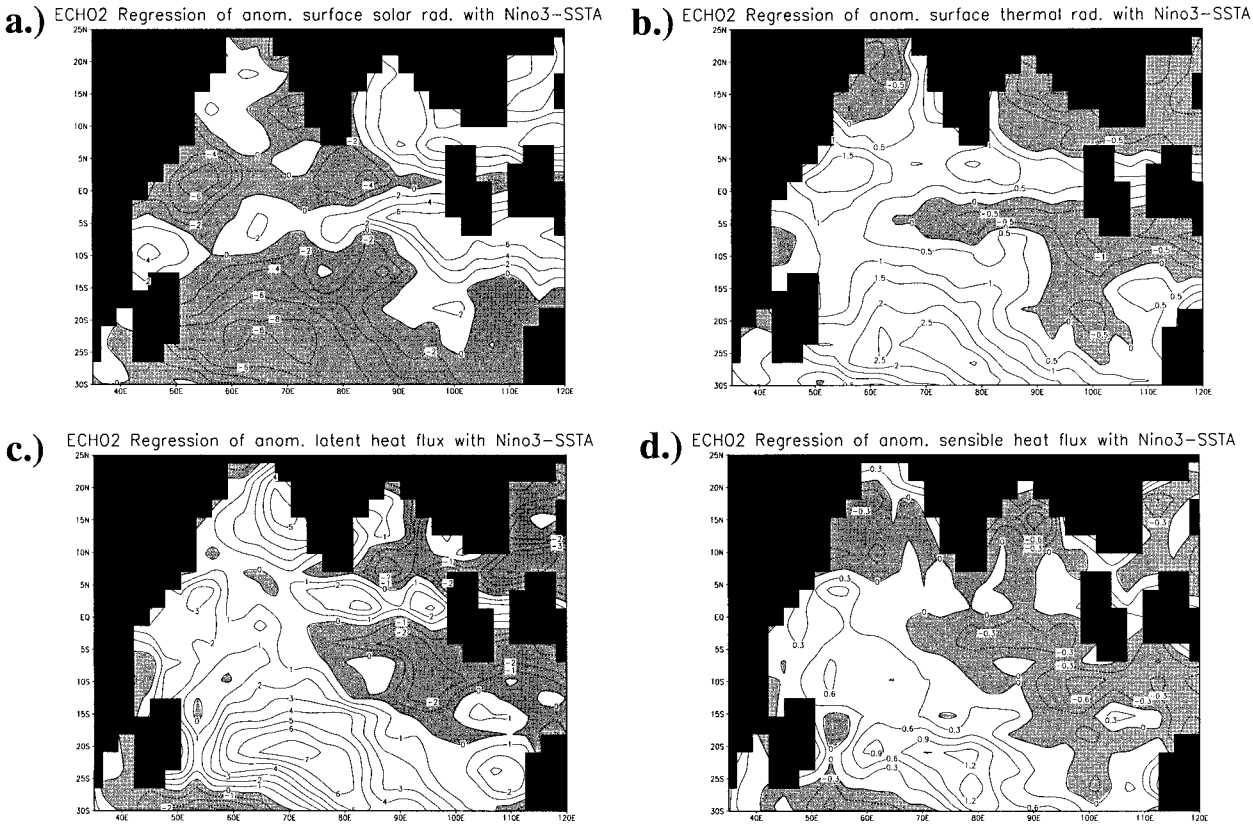

FIG. 12. Same as Fig. 6 but separately for the different surface heat flux components: (a) solar heat flux, (b) thermal heat flux, (c) latent heat, and (d) sensible heat flux [W $(m^2\ K)^{-1}$].

zonal component, on the other hand, shows prevailing westerly winds with maxima during the monsoon transition phases (Mc Phaden 1982). This does not change during ENSO extremes, even though easterly wind stress anomalies are found during warm ENSO phases (Figs. 7 and 13). Therefore, the easterly wind stress anomalies do not cause equatorial upwelling that would cool down the SSTs during warm ENSO phases. Instead, the anomalies in the velocity fields indicate that the reduced wind speed is associated with reduced vertical mixing, which leads to the warm SST anomalies that are found in the central equatorial Indian Ocean during warm ENSO phases. Therefore, the ENSO-induced SST changes in the central equatorial Indian Ocean are, at

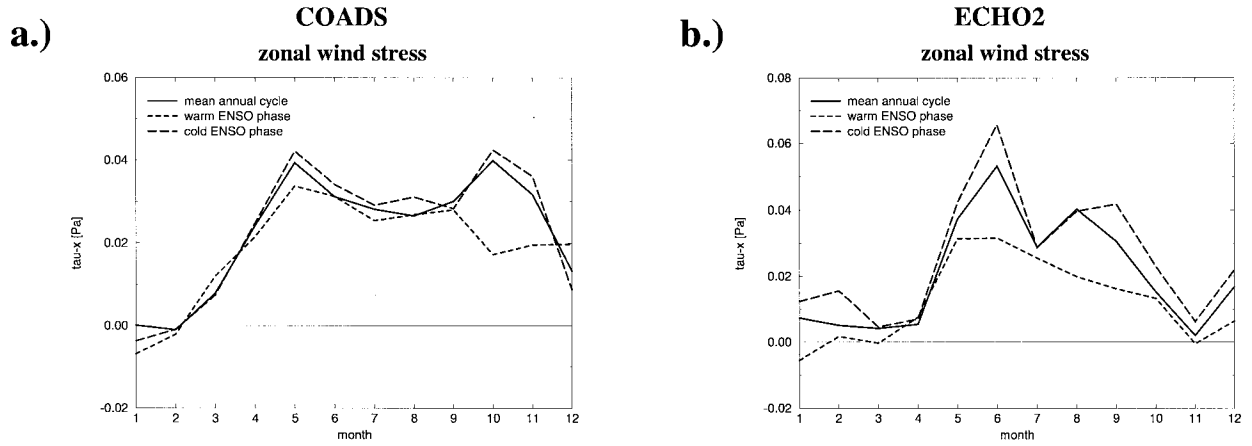

FIG. 13. Composite seasonal evolution of (a) observed and (b) simulated monthly mean zonal wind stress at 0°N, 75°–85°E for warm and cold ENSO phases.

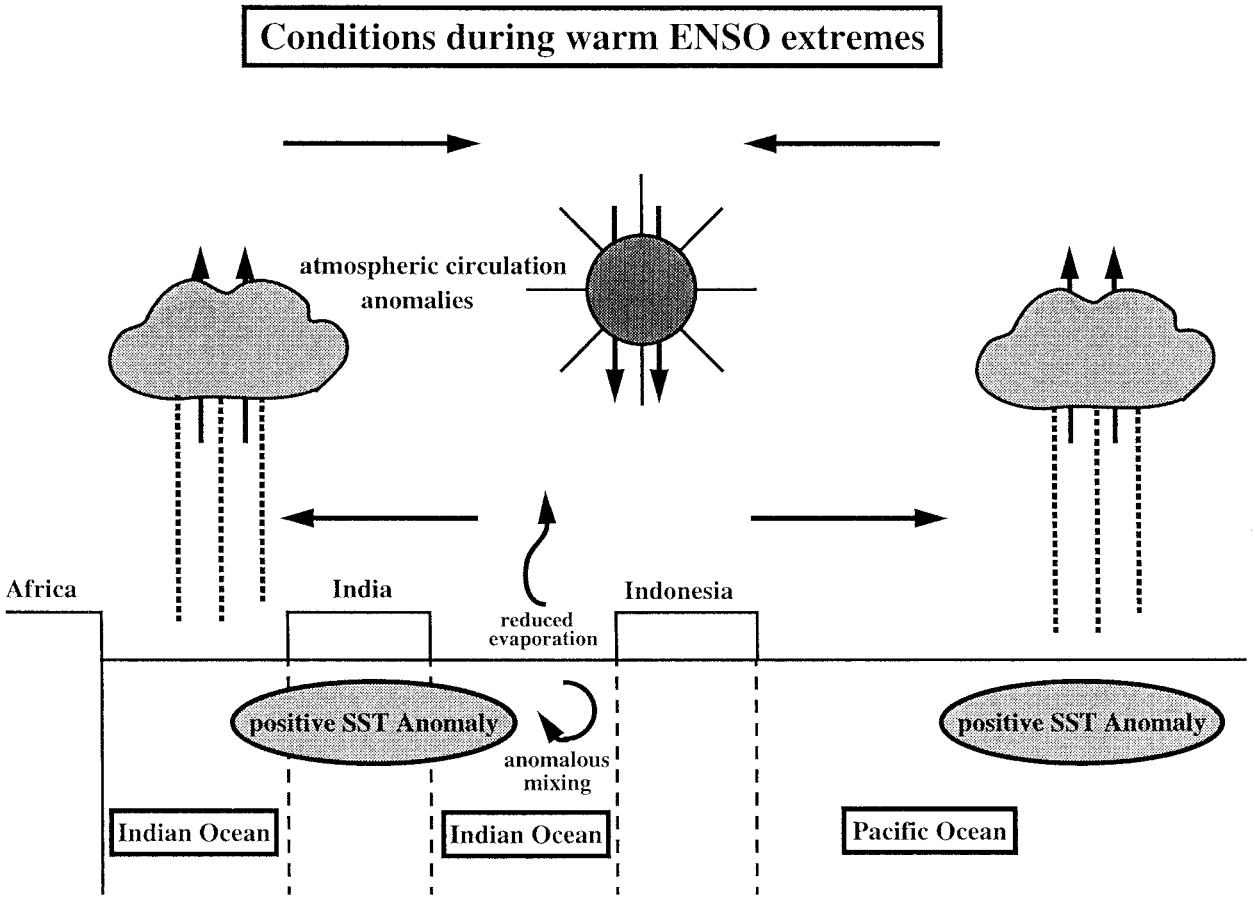

FIG. 14. Schematic diagram of conditions in the equatorial Indian Ocean region that prevail during warm ENSO extremes.

least partly, due to changes of vertical mixing, which are associated with the changed wind speed.

Furthermore, the dynamical response of the Indian Ocean to ENSO-related wind stress anomalies has to be considered. While we did not see any propagation of waves through the Indonesian Throughflow in our model, ENSO-related Rossby waves were found to be excited by local wind stress changes at about 10°S. However, they appear to have only a local impact on the SSTs in the Somali basin.

In a recent study Murtugudde and Bussalacchi (1999) have reached a different conclusion. They demonstrated with a reduced gravity, primitive equation ocean circulation model that while the heat flux is important in determining the observed interannual variability in the Indian Ocean, the wind forcing also contributes a significant component of the variability.

5. Summary

We have shown that the coupled ocean–atmosphere GCM ECHO-2 is capable of simulating realistically interannual variability in the tropical Pacific and the related variability in the Indian Ocean. Furthermore, we have shown that the interannual Indian Ocean SST variations in both the observations and our CGCM integration are strongly related to ENSO. About 4 months after large-scale SST anomalies are observed in the equatorial Pacific, the whole tropical and subtropical Indian Ocean is covered with anomalous SSTs of the same sign. As summarized in Fig. 14, the ENSO signal is mainly introduced into the Indian Ocean by a changed atmospheric circulation forced by the equatorial Pacific SST anomalies. In the integration with ECHO-2, the overall Indian Ocean warming during warm ENSO extremes is mainly due to surface heat flux changes. This has been speculated in earlier studies (e.g., Kiladis and Diaz 1989) but not studied in detail bacause of the lack of accurate observational data. The CGCM integration enabled us to investigate the lead–lag relationship between the Indian Ocean and the eastern Pacific Ocean SSTs as well as the relative importance of the different surface heat flux components. We found that in the eastern part of the equatorial Indian Ocean the anomalous solar radiative flux is the dominant agent in changing the SST. This can be understood as the result of the eastward movement of the ascending branch of the Walker circulation. The latent heat flux has the strongest

impact over the western and central basin where changes in the wind speed are strongest. Besides the surface heat flux forcing, anomalous winds also affect the SSTs in the central equatorial region by changing the vertical mixing and excite Rossby waves at about 10°S. The impact of the latter needs to be further investigated.

Acknowledgments. We would like to thank Prof. L. Bengtsson and his group for developing and providing the ECHAM-4 model, Dr. E. Maier-Reimer for helping in developing the HOPE-2 model, and Dr. H. Frey for setting up the coupled model and conducting the integration. Furthermore, thanks are due to G. Hildebrandt for processing the data. This work was sponsored by the European Union through the PROVOST and SINTEX projects and the German government through the Klimavariabilität und Signalanalyse project. The CGCM integration was performed at the Deutsches Klimarechenzentrum.

REFERENCES

Arakawa, A., and V. R. Lamb, 1977: Computational design of the basic dynamical processes of the UCLA general circulation model. *Method Comput. Phys.,* **17,** 173–265.

Chertock, B., R. Frouin, and R. C. Somerville, 1991: Global monitoring of net solar irradiance at the ocean surface: Climatological variability and the 1982–1983 El Niño. *J. Climate,* **4,** 639–650.

da Silva, A. M., C. C. Young, and S. Levitus, 1994: *Atlas of Surface Marine Data.* NODC, NOAA/NESDIS E/OC21, 416 pp.

Frey, H., M. Latif, and T. Stockdale, 1997: The coupled GCM ECHO-2. Part I: The tropical Pacific. *Mon. Wea. Rev.,* **125,** 703–720.

Grötzner, A., M. Latif, and T. P. Barnett, 1998: A decadal climate cycle in the North Atlantic Ocean as simulated by the ECHO coupled GCM. *J. Climate,* **11,** 831–847.

Ju, J., and J. M. Slingo, 1995: The Asian monsoon and ENSO. *Quart. J. Roy. Meteor. Soc.,* **121,** 1133–1168.

Kiladis, G. N., and H. F. Diaz, 1989: Global climatic anomalies associated with extremes in the Southern Oscillation. *J. Climate,* **2,** 1069–1090.

Latif, M., and T. P. Barnett, 1994: Causes of decadal climate variability over the North Pacific and North America. *Science,* **266,** 634–637.

——, and ——, 1995: Interactions of the tropical oceans. *J. Climate,* **8,** 952–964.

——, and ——, 1996: Decadal climate variability over the North Pacific and North America: Dynamics and predictability. *J. Climate,* **9,** 2407–2423.

——, T. Stockdale, J. Wolff, G. Burgers, E. Maier-Reimer, M. Junge, K. Arpe, and L. Bengtsson, 1994: Climatology and variability in the ECHO coupled GCM. *Tellus,* **46A,** 351–366.

Levitus, S., 1982: *Climatological Atlas of the World Ocean.* NOAA Prof. Paper 13, 173 pp. and 17 microfiche.

McPhaden, M. J., 1982: Variability in the central equatorial Indian Ocean. Part I: Ocean dynamics. *J. Mar. Res.,* **40,** 157–176.

Murtugudde, R., and A. Busalacchi, 1999: Interannual variability of the dynamics and thermodynamics of the tropical Indian Ocean. *J. Climate,* **12,** 2300–2326.

——, R. Seagar, and A. Busalacchi, 1996: Simulation of the tropical oceans with an ocean GCM coupled to an atmospheric mixed-layer model. *J. Climate,* **9,** 1795–1815.

Nicholls, N., 1989: Sea surface temperatures and Australian winter rainfall. *J. Climate,* **2,** 965–973.

Pierce, D. W., T. P. Barnett, and M. Latif, 2000: Connections between the Pacific Ocean Tropics and midlatitudes on decadal timescales. *J. Climate,* **13,** 1173–1194.

Philander, S. G., 1990: *El Niño, La Niña and the Southern Oscillation.* Academic Press, 293 pp.

Reverdin, G., 1987: The upper equatorial Indian Ocean: The climatological seasonal cycle. *J. Phys. Oceanogr.,* **17,** 903–927.

Reynolds, R. W., 1988: A real-time global sea surface temperature analysis. *J. Climate,* **1,** 75–86.

Roeckner, E., and Coauthors, 1996: The atmospheric general circulation model ECHAM-4: Model description and simulation of the present day climate. Rep. 218, Max-Planck-Institut für Meteorologie, 90 pp. [Available from MPI für Meteorologie, Bundesstr. 55, 20146 Hamburg, Germany.]

Schneider, N., T. Barnett, M. Latif, and T. Stockdale, 1996: Warm pool physics in a coupled GCM. *J. Climate,* **9,** 219–239

Shukla, J., 1987: Interannual variability of monsoons. *Monsoons,* J. S. Fein and P. L. Stephens, Eds., Wiley and Sons, 399–463.

Soman, M. K., and J. M. Slingo, 1997: Sensitivity of the Asian summer monsoon to aspects of sea-surface-temperature anomalies in the tropical Pacific Ocean. *Quart. J. Roy. Meteor. Soc.,* **123,** 309–336.

Villwock, A., 1994: ENSO induced variability in the India Ocean (in German). Ph.D. thesis, Max Planck Institute, 80 pp. [Available from MPI für Meteorologie, Bundesstr. 55, 20146 Hamburg, Germany.]

Webster, P. J., 1990: Ocean–atmosphere interaction in the Tropics. *Proc. 1990 ECMWF Annual Seminar: Tropical Extra-Tropical Interactions,* Reading, United Kingdom, ECMWF, 67–119.

——, and S. Yang, 1992: Monsoon and ENSO: Selectively interactive systems. *Quart. J. Roy. Meteor. Soc.,* **118,** 877–926.

Wolff, J.-O., E. Maier-Reimer, and S. Legutke, 1997: HOPE, The Hamburg Ocean Primitive Equation Model. Tech Rep., 98 pp. [Available from DKRZ, Bundesstr. 55, 20146 Hamburg, Germany.]

Wyrtki, K., 1973: An equatorial jet in the Indian Ocean. *Science,* **181,** 242–254.